

First-Principles Prediction of Possible Rare-Earth Free Permanent Magnet of Tetragonal FeCo with Enhanced Magnetic Anisotropy and Energy Product through Interstitial Nitrogen

Dorj Odkhuu^{1,*} and Soon Cheol Hong^{2,†}

¹Department of Physics, Incheon National University, Incheon 22012, South Korea

²Department of Physics, University of Ulsan, Ulsan 44610, South Korea

(Received 23 January 2019; revised manuscript received 28 March 2019; published 30 May 2019)

Pushing a uniaxial magnetic anisotropy (K_u) up to an order of meV per atom in bulk structures composed of only $3d$ magnetic elements with large saturation magnetization ($\mu_0 M_s$) and Curie temperature (T_c) has been a long-term goal of hard permanent magnet and spintronics studies. Herein, using *ab initio* calculations, we predict an unexpectedly large K_u up to 1/2 meV/formula unit in B2-ordered tetragonal FeCo, which is even comparable to or more than 50% of those for the currently known permanent magnetic materials with $4d$, $5d$, and $4f$ orbitals. This large K_u is associated with an interplay mechanism of the Jahn-Teller-like tetragonal distortion induced by doping with an interstitial $2p$ -electron element, herein nitrogen as an example, and the strong orbital hybridization between $3d$ and $2p$ states. Our findings demonstrate the feasibility of significant enhancements on the magnetic anisotropy and energy product of $3d$ magnetic metals through the interstitial doping with $2p$ -electron nonmetal elements.

DOI: 10.1103/PhysRevApplied.11.054085

I. INTRODUCTION

The recent development in rare-earth free permanent magnet and spintronics research fields requires breakthrough that pushes a uniaxial magnetic anisotropy (K_u) beyond. In particular, there have been tremendous efforts to enhance K_u up to an order of meV per atom in $3d$ magnetic metals, which possess large saturation magnetization ($\mu_0 M_s$) and Curie temperature (T_c), without the inclusions of $4d$ -to- $5d$ heavy transition metal (TM) or $4f$ rare-earth (RE) elements. Researchers have focused on body-centered cubic (bcc) Fe and FeCo alloys to address this issue, because of their relatively cheap cost and simple fabrication compared with other commercial hard magnetic materials, including CoPt(Pd) and FePt(Pd) [1–4].

Despite their large $\mu_0 M_s$ and high T_c , however, such a high-symmetry cubic structure exhibits a very small K_u , typically in the order of μeV per atom. Moreover, in these $3d$ magnetic metals, the absolute value of K_u is largely limited by the intrinsic natures of weak spin-orbit coupling (SOC) and orbital angular momentum (L). Thus, a favorable approach to enhancing K_u resides in reducing symmetry as the energy levels of d orbitals evolve in different crystal symmetries [5]. Such a modification of the energy levels of d orbitals, particularly around the Fermi level (E_F), in turn, determines K_u according to the

perturbation theory [6,7]. Herewith, for the bcc lattice ($c/a = 1$) of Fe or B2-ordered FeCo, the cubic symmetry splits five d orbitals into doublets (e_g) and triplets (t_{2g}) [Fig. 1(a)]. When the symmetry decreases ($c/a \neq 1$), additional Jahn-Teller-like splitting offers a greater degree of electronic-energy-level freedom. More specifically, the tetragonal distortion further splits these e_g and t_{2g} levels into two irreducible representations: e_g into two singlets $a_1(d_{x^2-y^2})$ and $b_1(d_{z^2})$ and t_{2g} into a singlet $b_2(d_{xy})$ and a doublet $e(d_{yz,xz})$, as illustrated in Fig. 1(b), where their relative order depends on whether c/a is greater or smaller than unity.

Based on this argument, an unexpectedly large K_u up to 0.8 meV/atom was first predicted in body-centered tetragonal (bct) FeCo with a c/a ratio of 1.20–1.25 and 60 at. % Co [8]. In subsequent experiments [9–11], such a tetragonal distortion in FeCo films has been well achieved by epitaxial growth techniques using lattice mismatching substrates, such as Pd(001) [9,10], Rh(001) [10], Ir(001) [10], and Pt(001) [11]. The strength of the tetragonal distortion (i.e., c/a ratio) and thereby the absolute value of K_u depend on the choices of the substrate and the film thickness of the FeCo sample and the concentration x in $\text{Fe}_{1-x}\text{Co}_x$. Furthermore, the induced tetragonal distortion in FeCo films is feasible only with a limited film thickness a few nanometers thick [9–11]. However, such a nanometer-scaled thickness is insufficient for the practical usage in permanent magnetic materials at the bulk scale.

*odkhuu@inu.ac.kr

†schong@ulsan.ac.kr

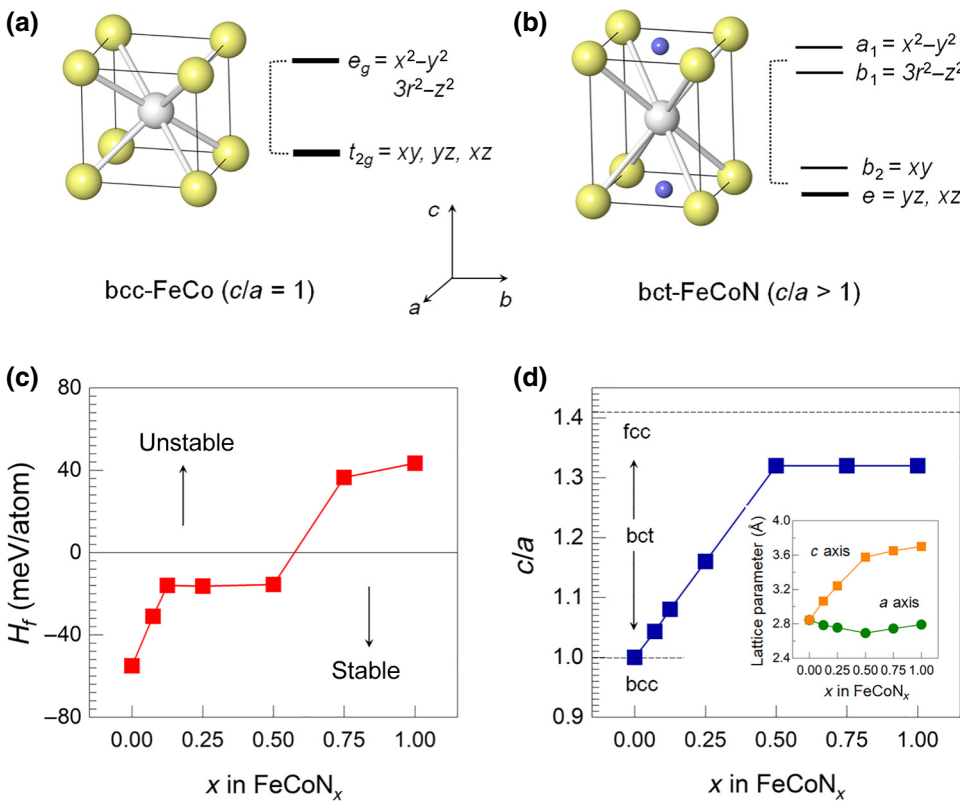


FIG. 1. (a),(b) Schematic presentation of the Jahn-Teller-like splitting of d -orbital energy levels of FeCo across the bcc-to-bct transition under N doping. In the atomic structure, while the yellow and white spheres represent the Fe and Co atoms, respectively, the smaller blue spheres are the N-dopant atoms. In the cubic symmetry (bcc with $c/a = 1$), the d orbitals split into the high-lying doublets (e_g) and low-lying triplets (t_{2g}). Tetragonal distortion (bct with $c/a > 1$) further splits e_g into a_1 and b_1 ; t_{2g} splits into a singlet b_2 and a doublet e . (c) The formation energy H_f and (d) tetragonal distortion c/a ratio of FeCoN_x as a function of x . In (d), the two horizontal dashed lines denote the c/a corresponding to the cubic phases, bcc ($c/a = 1$) and fcc ($c/a = 1.41$). The inset shows the optimized lattice parameters a (circle) along the short axis and c (square) along the long axis.

In this paper, we propose a promising approach that leads to the possibility of breaking the high-symmetry cubic lattice of B2-ordered FeCo in bulk form by interstitially doping with $2p$ -electron elements, in N as an example. The resulting tetragonal phase of FeCoN_x alloys, where x is the relative atomic ratio of an interstitial N to Fe (or Co) in the formula unit (f.u.) cell, exhibits an unexpectedly large uniaxial K_u up to approximately 0.5 meV/f.u. with the easy magnetization axis along the long-axis direction. The underlying mechanism is discussed in terms of the energy level changes in two short-axis d -orbital states, d_{xy} and $d_{x^2-y^2}$, which are coupled by SOC, driven by the Jahn-Teller-like tetragonal distortion and the strong $3d$ - $2p$ hybridization. In addition, the exchange interaction and Curie temperature are estimated in connection with the mean-field approximation.

II. METHODOLOGY

We use density functional theory (DFT) calculations within the projector-augmented-wave (PAW) pseudopotential method [12], as implemented in the Vienna *ab initio* simulation package (VASP) [13]. The exchange correlation functional is treated with the generalized gradient approximation (GGA) by Perdew, Burke, and Ernzerhof (PBE) [14]. The primitive unit cell structures of $1 \times 1 \times 1$ B2-ordered FeCo ($x = 0$) and FeCoN ($x = 1$) are shown in Figs. 1(a) and 1(b), respectively. For FeCoN_x with

$x = 0.074, 0.125, 0.25, 0.5$, and 0.75 , $2 \times 2 \times 2$ (16-atom FeCo) and $3 \times 3 \times 3$ (54-atom FeCo) supercells are adopted. In the supercell structure, the N is embedded as interstitial doping, as the dissolved N or B atoms occupy the octahedral interstices in experiments for $(\text{FeCo})_{16}\text{N}_2$ [15,16], $(\text{Fe}_{0.7}\text{Co}_{0.3})_{1-x}\text{B}_x$ [17], and $\alpha''\text{-Fe}_{16}\text{N}_2$ samples [18]. There are two distinguishable interstitial sites in B2 FeCo: the octahedron center surrounded by 4 Fe and 2 Co (denoted as a 4-Fe coordinated octahedron) and the octahedron center surrounded by 4 Co and 2 Fe (4-Co coordinated octahedron). Our calculations show that the 4-Fe coordinated octahedron is more favored than the 4-Co coordinated one by an energy difference of about 0.5 eV/N, in agreement with the previous calculations [19]. For each x , we then consider various possible distribution patterns of the N dopant atoms within the 4-Fe octahedron and results shown in the following paragraphs refer to the most favorable phase. More specifically, the N dopant atoms prefer the 4-Fe coordinated octahedron with the Fe atoms lying on the (001) plane (or a - b plane), rather than the simultaneous two interstitial sublattices on the (001) and (100)/(010) plane (or a - c / b - c plane), in uniform distribution over a unit cell. As an example, we show five different distributions of the interstitial N atoms in $3 \times 3 \times 3$ unit cells of $\text{FeCoN}_{0.074}$ in Fig. 2: (a) first nearest neighbor (1NN) 4-Fe coordinated octahedrons with the Fe atoms lying on the (001) plane, denoted as 1NN 4-Fe@(001); (b) second NN 4-Fe coordinated octahedrons with the Fe atoms lying

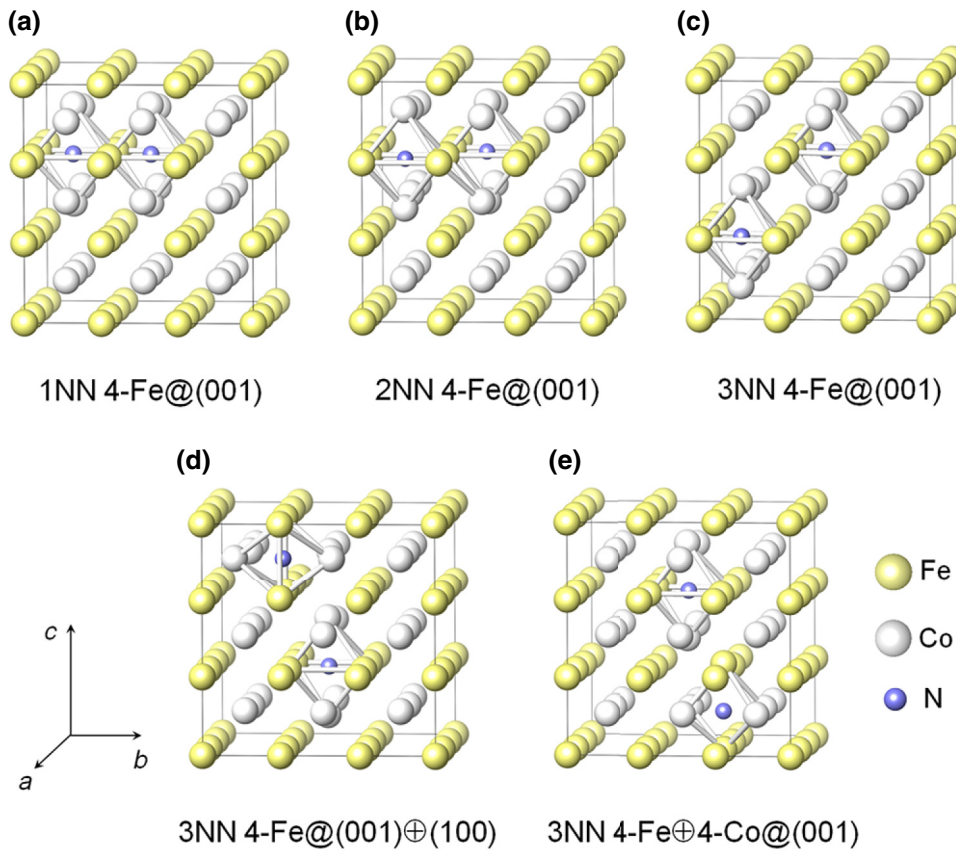


FIG. 2. (a)–(e) Different distributions of the interstitial N-dopant atoms in $3 \times 3 \times 3$ unit cells of FeCoN_x when $x = 0.074$. The notation of the atomic symbol is the same as used in Fig. 1. In each configuration, the octahedrons with the N-dopant atom at the center are indicated.

on the (001) plane [2NN 4-Fe@(001)]; (c) third NN 4-Fe coordinated octahedrons with the Fe atoms lying on the (001) plane [3NN 4-Fe@(001)]; (d) third NN 4-Fe coordinated octahedrons with the Fe atoms lying on the (001) and (100) plane [3NN 4-Fe@(001) \oplus (100)]; and (e) third NN 4-Fe coordinated and 4-Co coordinated octahedrons [3NN 4-Fe \oplus 4-Co@(001)]. The relative energies of 1NN 4-Fe@(001), 2NN 4-Fe@(001), 3NN 4-Fe@(001) \oplus (100), and 3NN 4-Fe \oplus 4-Co@(001) with respect to the most stable 3NN 4-Fe@(001) are approximately 0.033, 0.028, 0.067, and 0.418 eV/N, respectively. For $2 \times 2 \times 2$ ($3 \times 3 \times 3$) supercells, we use an energy cutoff of 500 eV and a $9 \times 9 \times 9$ ($5 \times 5 \times 5$) k -point mesh to relax the structures and ionic coordinates until the largest force acting on each atom becomes less than 10^{-2} eV/ \AA . The Gaussian smearing method with a small smearing (0.05 eV) and dense k points ($15 \times 15 \times 15$) are used in the noncollinear calculations for the $2 \times 2 \times 2$ supercell, which are sufficient to provide well-converged values of K_u . The SOC term is included in a second-variational way employing scalar-relativistic calculations of the valence states [20].

III. RESULTS AND DISCUSSION

The structural phase stability of B2-ordered FeCo, upon the addition of N-dopant atoms, is first explored. The phase stability versus phase decomposition into end member

compounds can be described thermodynamically by the change in the Gibbs free energy [21,22],

$$\Delta G(T, P, N_i) = \Delta H(T, P, N_i) - T\Delta S(T, P, N_i) + P\Delta V(T, P, N_i), \quad (1)$$

where H is the total energy of the system and T, S, P , and V are the temperature, entropy, pressure, and volume of the system, respectively. N_i is the number of atom species i (i.e., $i = \text{Fe}, \text{Co}, \text{and N}$) in the unit cell. We follow a recipe proposed by Ong *et al.* [21,22], where the compositional phase diagram can be constructed using the convex hull with the condition $T = 0$ K. On the other hand, the $P\Delta V$ term is relatively small and thus usually neglected. Thus, as $\Delta G = \Delta H$ at 0 K, the formation energy (H_f) can be formulated as

$$H_f = \frac{H_{\text{compound}} - \sum_i \mu_i N_i}{\sum_i N_i} \quad (2)$$

where μ_i is the chemical potential of atom species i . The chemical potential μ_i can be estimated as the total energy of the elemental ground state at 0 K.

The calculated H_f of FeCoN_x as function of x is shown in Fig. 1(c). The negative H_f means the favorable formation of the single crystalline structure of FeCoN_x against the phase separation into the bulk phases of its constituent

elements, i.e., bcc-Fe, hcp-Co, and N₂ in the gas phase. For FeCo, the cubic ($c/a = 1$) is the most stable structure as B2 is the ground-state phase, where H_f is about -55 meV/atom. For FeCoN_x, the magnitude of H_f decreases as x increases and changes its sign to positive at $x = 0.5\text{--}0.75$. Thus, the B2-ordered phase of FeCo is still energetically stable upon the N doping with no more than 1/2 N-atom/f.u., which corresponds to 20 at. % N. Since the formation affinity computed in the present study is valid only at 0 K, an acceptable amount of the N dopants in practice would be more limited at an elevated temperature. Experiments, for instance, reported that Fe_{0.9}Co_{0.1} [15] and α -Fe [18] can accommodate the N dopants up to 12.5 at. % and still retain their α phase but with significant tetragonal distortion (i.e., bct). Furthermore, it is experimentally shown that the stability of the α'' -Fe₁₆N₂ phase can be substantially enhanced by a Co addition [16]. We thus expect that in low-temperature experiments the amount of the N dopants could reach or even exceed more than 12.5 at. % N in FeCo with 50 at. % Co.

In Fig. 1(d), we show the tetragonal distortion c/a ratio of FeCoN_x for the different x . The inset shows the corresponding lattice parameters a along the short axis and c along the long axis. Our optimized a of FeCo in its

ground-state B2 phase is 2.844 Å, in good agreement with the previous theories [23,24] and experiments [25]. The N addition further expands the lattice along the c axis, by up to approximately 25% ($c = 3.58$ Å), but reduces a up to 2.69 Å at $x = 0.5$. As a result, the c/a ratio increases linearly with x , reaching the largest value of 1.32 at $x = 0.5$, and remains the same for $x > 0.5$. Notably, such an induced tetragonal distortion of FeCo by the N doping is indeed substantial to yield a considerable K_u therein, as addressed later. We would like to further note that the obtained c/a values of 1.1–1.3 at $x = 0.125\text{--}0.5$ (or 6–20 at. % N) would be optimal, at least in our objective of interest; otherwise, one acquires another high-symmetry phase, i.e., face-centered cubic (fcc), as c/a increases further to 1.41. As indicated in Fig. 1(d), the atomic structure of FeCo undergoes a phase transition from bcc to bct upon the small addition of N and tends to transform to a fcc phase at large x .

Figure 3(a) shows the total spin magnetic moment (m_s) per f.u. and atom-projected moment (m_s^X), for FeCoN_x. The B2 FeCo exhibits a highest m_s of $4.54\mu_B$ /f.u., where m_s^{Fe} and m_s^{Co} are 2.78 and $1.76\mu_B$, respectively. Our results reproduce those reported in experiments [25–27] and previous theories [8,19,23,24,28]. Both the Fe and Co

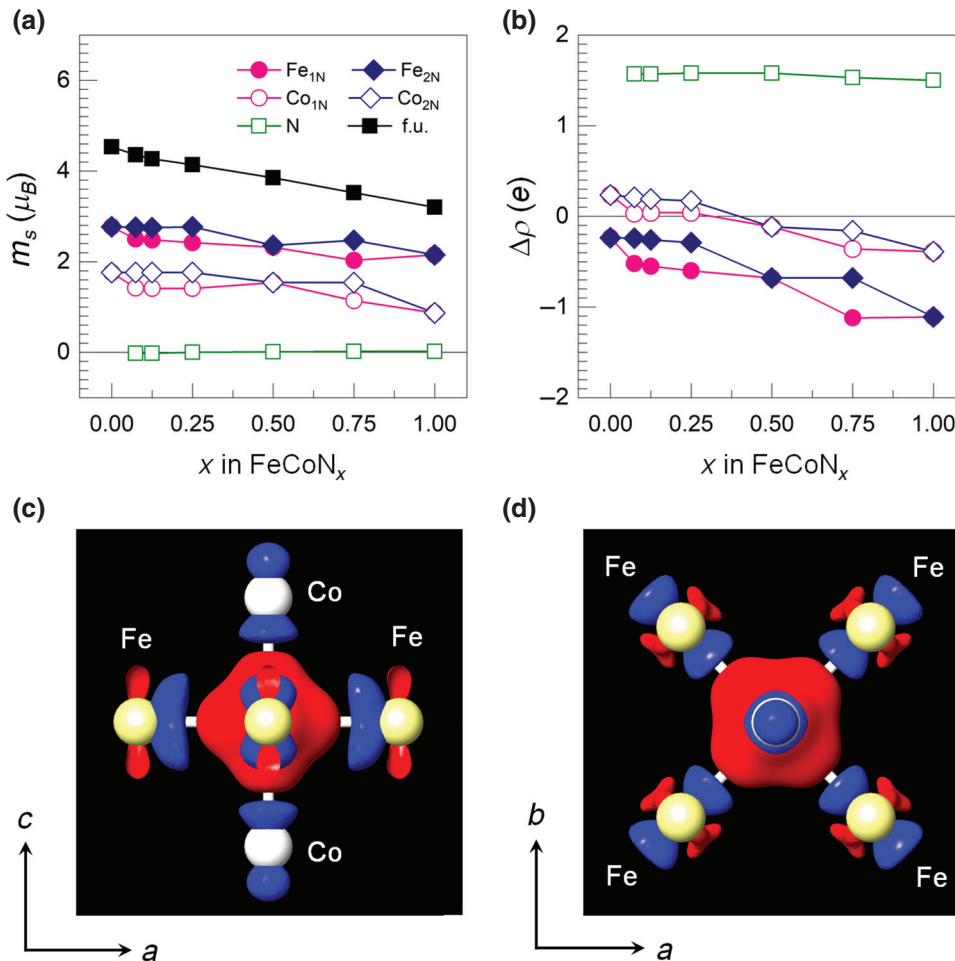


FIG. 3. (a) Spin magnetic moment m_s and (b) charge difference $\Delta\rho$ of the Fe, Co, and N atoms in FeCoN_x as function of x . In (a), the total magnetic moment per formula unit cell (f.u.) is also shown in the filled square. (c) Side and (d) top view of the isosurface plot of the charge redistribution ΔQ for $\text{FeCoN}_{0.125}$. For simplicity, only the octahedron centered at the dopant N site surrounding by the 4 Fe (yellow spheres) on the $a\text{-}b$ plane and 2 Co atoms (white spheres) along the c axis are shown. Red and blue isosurfaces correspond to the charge accumulation and depletion in units of 5×10^{-2} e/bohr³, respectively.

moments in FeCoN_x decrease with x , resulting in reduced magnetization to $4.17\mu_B/\text{f.u.}$ at the practically acceptable (i.e., $x = 0.25$ or 11.1 at. % N) and $3.90\mu_B/\text{f.u.}$ at the upper limit of N contents, $x = 0.5$ or 20 at. % N. Note that, even at the theoretically acceptable range of N at 0 K (≤ 20 at. % N), the magnetic moments of all Fe and Co sites are still higher or comparable with those of bulk bcc-Fe ($2.2\mu_B$) and hcp-Co ($1.6\mu_B$). Overall, our results of $4.54\text{--}3.90\mu_B/\text{f.u.}$ (or $\mu_0M_s = 2.3\text{--}1.8\text{ T}$) at $x = 0\text{--}0.5$ are greater by more than 10%, compared with the current best permanent magnet $\text{Nd}_2\text{Fe}_{14}\text{B}$ (1.61 T) [29]. The decrement in magnetism is mainly due to the suppressed magnetic moments of the 1NN Fe and Co atoms to the N site, which we denote as $\text{Fe}_{1\text{N}}$ and $\text{Co}_{1\text{N}}$. On the other

hand, the magnetic moments of the 2NN Fe and Co to the N site ($\text{Fe}_{2\text{N}}$ and $\text{Co}_{2\text{N}}$) almost preserve those in FeCo. A similar phenomenon is found in previous full-potential calculations for C and N-doped FeCo [23,30]. These reduced moments of the $\text{Fe}_{1\text{N}}$ and $\text{Co}_{1\text{N}}$ atoms can be understood by the charge transfer/redistribution [19] and the Fe(Co) $3d$ -N $2p$ hybridization [23,31], as discussed in the following paragraphs. In addition, induced moments at the N-dopant sites are rather small, of the order of $0.01\text{--}0.02\mu_B$.

We show the relative charge ($\Delta\rho$) with respect to the nominal charge in Fig. 3(b). The nominal charges of Fe, Co, and N atoms in their bulk forms are 8, 9, and 5 e^- , respectively. For better analyses, we illustrate the a - c and a - b plane projected electron redistribution maps,

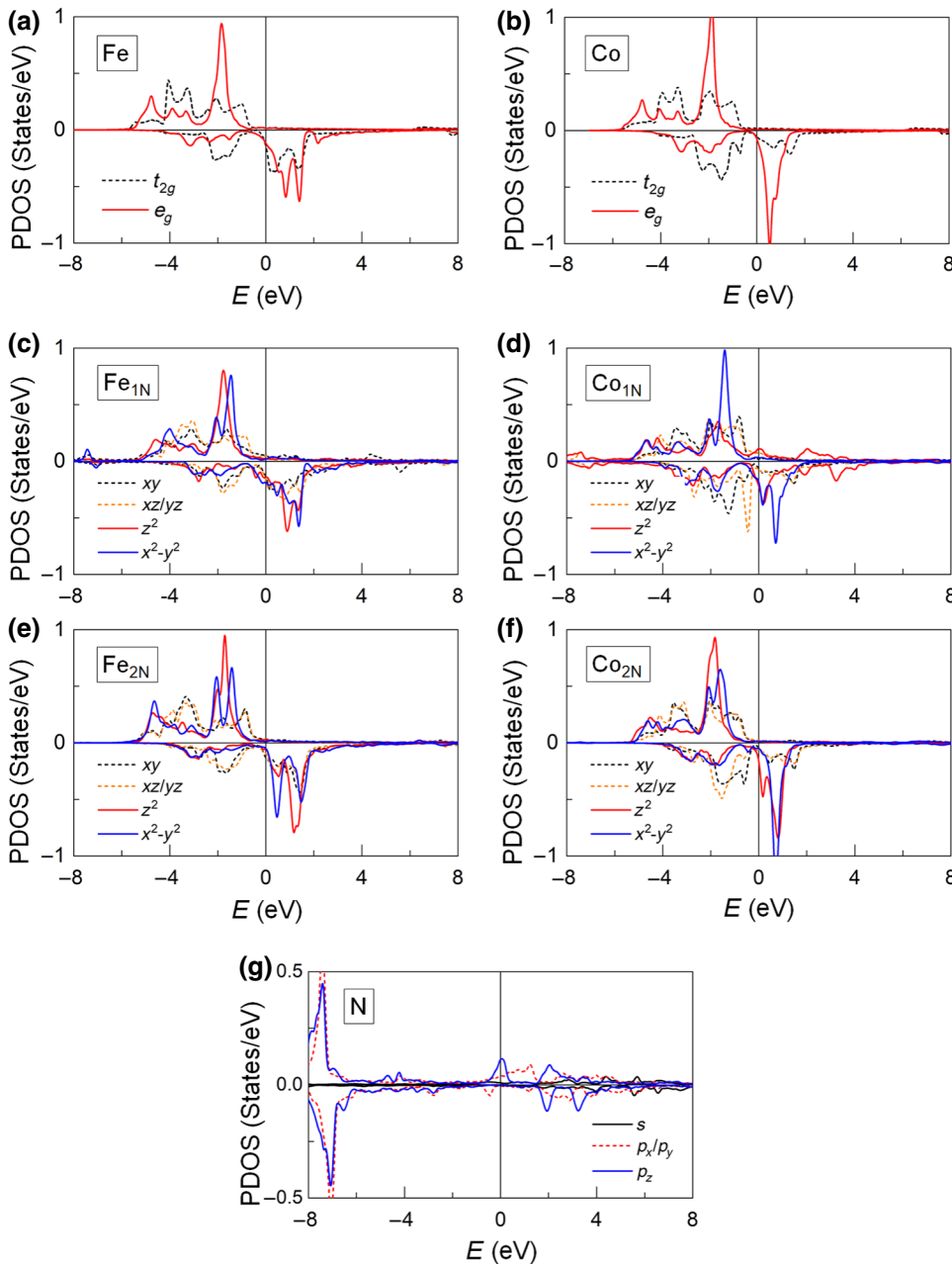


FIG. 4. The d -orbital PDOS of the (a) Fe and (b) Co atoms for B2 FeCo. The same for the (c) $\text{Fe}_{1\text{N}}$, (d) $\text{Co}_{1\text{N}}$, (e) $\text{Fe}_{2\text{N}}$, and (f) $\text{Co}_{2\text{N}}$ atoms for $\text{FeCoN}_{0.125}$. (g) The s - and p -orbital PDOS of the N-dopant atom for $\text{FeCoN}_{0.125}$. The Fermi level is set to zero energy.

$\Delta Q = Q(\text{FeCoN}_x) - Q(\text{FeCo}) - xQ(\text{N})$, in Figs. 3(c) and 3(d) for $\text{FeCoN}_{0.125}$, respectively. For FeCo, the charge transfer of 0.24 e occurs from Fe to Co because of the larger electronegativity of Co (1.9) than Fe (1.8). This result is a consequence of the upward shift of the minority-spin states of Fe toward the high-energy region across E_F due to the Fe d -Co d hybridization, which explains the enhanced moment of Fe in FeCo with respect to its bulk value ($2.2\mu_B$). For FeCoN_x , the calculated $\Delta\rho$ exhibits a trend similar to m_s ; the $\Delta\rho$ decreases with x for both Fe and Co. Consequently, a significant amount of charge of 1.5–1.6 e is accumulated in the N-dopant site, regardless of the doping concentration. The electronegativity is much larger in N (3.0) than in Fe and Co. In particular, the $\text{Fe}_{1\text{N}}$ and $\text{Co}_{1\text{N}}$ atoms deplete more charge to the N-dopant site than the $\text{Fe}_{2\text{N}}$ and $\text{Co}_{2\text{N}}$ [Figs. 3(b)–3(d)]. In the analyses below, this charge transfer occurs mainly in the majority-spin electronic state, which in turn reduces the spin exchange splitting of Fe and Co atoms.

Figures 4(a) and 4(b) show the partial density of states (PDOS) of the Fe and Co d -orbital states for B2 FeCo, respectively. In B2 FeCo, the cubic symmetry splits the Fe and Co d -orbital states into doublets (e_g) and triplets (t_{2g}). For both Fe and Co, these $3d$ states are completely filled in the majority-spin states, while the minority-spin states are divided into the occupied and unoccupied two major parts. In particular, the Co t_{2g} states have more occupancies in the

minority-spin states than the Fe t_{2g} , as Co holds one more electron than Fe in an ideal case. Thus, the spin moment difference of approximately $1\mu_B$ between the Fe and Co sites is mainly associated with the dissimilar energy levels in the minority-spin low-lying t_{2g} states.

In tetragonal symmetry, the e_g and t_{2g} states split into two singlets a_1 ($d_{x^2-y^2}$) and b_1 (d_{z^2}) and one singlet b_2 (d_{xy}) and one doublet e ($d_{xz,yz}$), respectively. However, in the presence of N- $2p$ electronic states, such a simple crystal field splitting not only affects the absolute value of the $3d$ energy levels, but also the hybridization between $3d$ and $2p$ orbital states. Obviously, from comparison in Figs. 4(c) and 4(d) of the $\text{Fe}_{1\text{N}}/\text{Co}_{1\text{N}}$ PDOS and Figs. 4(e) and 4(f) of the $\text{Fe}_{2\text{N}}/\text{Co}_{2\text{N}}$ -PDOS, the orbital hybridization between the $\text{Fe}_{1\text{N}}/\text{Co}_{1\text{N}}$ - $3d$ and N- $2p$ states is evident. Both the majority- and minority-spin $3d$ states of the $\text{Fe}_{1\text{N}}$ and $\text{Co}_{1\text{N}}$ atoms are broadened compared to the corresponding states of $\text{Fe}_{2\text{N}}$ and $\text{Co}_{2\text{N}}$. In particular, as produced by the $3d$ - $2p$ hybridization, the dense minority-spin PDOS- $d_{x^2-y^2}$ states of the $\text{Fe}_{1\text{N}}$ [Fig. 4(c)] and $\text{Co}_{1\text{N}}$ [Fig. 4(d)] and the majority-spin N- p states [Fig. 4(g)] across E_F are most prominent.

The N-doping driven bcc-bct transition accompanies an extremely large uniaxial K_u . The calculated K_u values of FeCoN_x are shown in Fig. 5(a) for the different x . Here, K_u is determined as $K_u = E_a - E_c$, where E_a and E_c are the total energies with magnetization along the

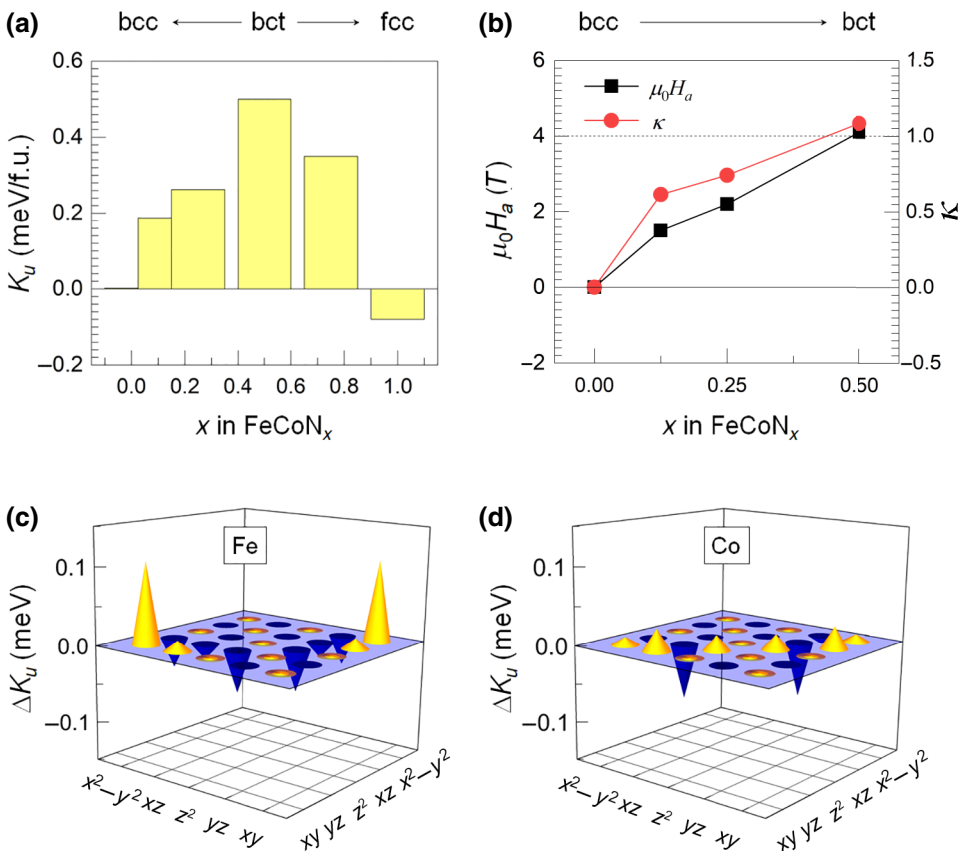


FIG. 5. (a) Uniaxial magnetic anisotropy K_u and (b) anisotropy field $\mu_0 H_a$ (square in left) and hardness parameter κ (circle in right) of FeCoN_x as a function of x . The dashed line in (b) corresponds to $\kappa = 1$, a threshold of the hard magnetic features. Changes of the d -orbital resolved K_u , ΔK_u , of the (c) Fe and (d) Co atoms in the presence of the N dopant for $\text{FeCoN}_{0.125}$. Yellow and blue bars represent the positive and negative ΔK_u , respectively.

a- and *c*-axis direction, respectively. The validity of this total energy estimation is also double checked with the force method [32]: $K_u = \sum_{o,k} [\varepsilon(n, k)_a - \varepsilon(n, k)_c]$, where $\varepsilon(n, k)_a$ and $\varepsilon(n, k)_c$ are the eigenvalues of occupied states in the Hamiltonian for the *a*- and *c*-axis magnetization, respectively. For B2 FeCo, the concept of uniaxial magnetic anisotropy between the *a* and *c* axis is not relevant, owing to their indistinguishable crystallographic lattices. For FeCoN_x, the K_u increases rapidly with *x* up to *x* = 0.5, reaching a maximum value of approximately 0.5 meV/f.u., and then decreases further. The positive sign in K_u stands for a uniaxial magnetic anisotropy with the easy magnetization along the long-axis (or *c*-axis) direction.

Our calculated K_u ranges from approximately 0.2 meV/f.u. at *c/a* = 1.1 to approximately 0.5 meV/f.u. at *c/a* = 1.32, which are roughly within the same order of 0.1–0.4 meV/atom at *c/a* = 1.1–1.25 in previous *ab initio*

calculations for the tetragonally distorted FeCo without N [8,33]. The authors mentioned that these values in FeCo are notably exceeded compared with the corresponding results for 4*d* Pd- and 5*d* Pt-included compounds, such as FePd, FePt, and CoPt (cf. Fig. 2 and references in Ref. [8]). On the other hand, in recent experiments [34], a K_u value of 2.1 MJ m⁻³ was reported in FeCo films with 10 at. % Al doping, where *c/a* = 1.21. This result is also within the range of our values of 1.5–3.0 MJ m⁻³ (or 0.26–0.49 meV/f.u.) at *c/a* = 1.16–1.32. We further would like to emphasize that K_u of FeCo with 20 at. % N is more than 60% of the measured value (4.5 MJ m⁻³) at 300 K for Nd₂Fe₁₄B (which is often referred to as the most efficient permanent magnet with large K_u thus far) [29].

As $\mu_0 M_s$ and K_u are known, we next determine the intrinsic hard magnetic properties such as anisotropic field H_a and hardness parameter κ . According to the empirical

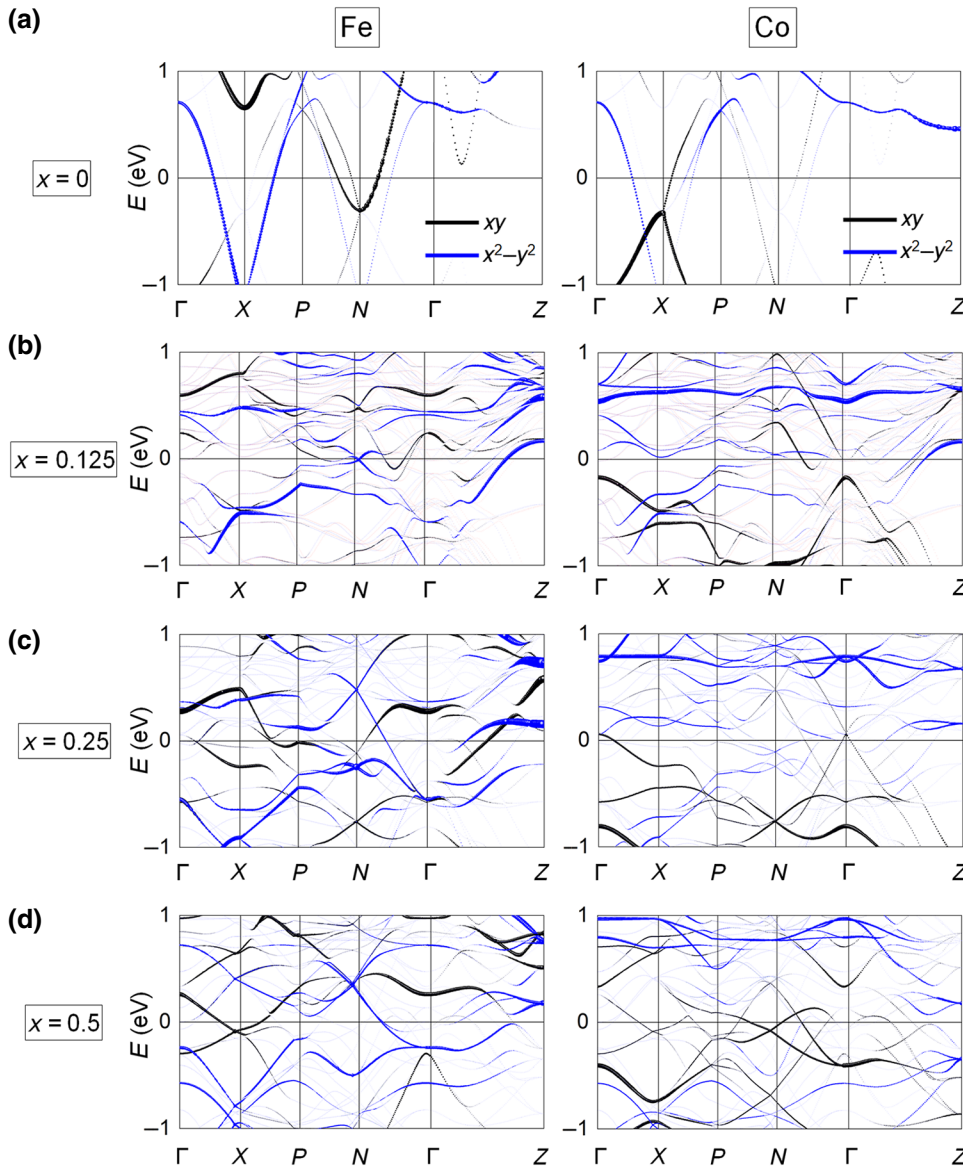


FIG. 6. (a) Energy- and *k*-resolved distribution of the d_{xy} (black) and $d_{x^2-y^2}$ (blue) orbital characters of the minority-spin bands for the Fe (left) and Co (right) atoms in B2 FeCo. The same for the Fe_{1-x} (left) and Co_{1-x} (right) of FeCoN_x for (b) *x* = 0.125, (c) 0.25, and (d) 0.5. The size of the symbols is proportional to their weights. The Fermi level is set to zero energy.

equation by Kronmüller *et al.* [35–37], the coercivity $\mu_0 H_c$ is given by

$$\mu_0 H_c = \alpha \mu_0 H_a - D_{\text{eff}} M_s, \quad (3)$$

where α is the microstructure constant and D_{eff} is an effective local demagnetizing factor. In most magnets, these parameters are scaled less than a value of 1, i.e., $\alpha < 1$ and $D_{\text{eff}} < 1$ [35,38,39], the absolute value of which depends on the shape and size of the grain, temperature, and other extrinsic quantities. On the other hand, as an intrinsic quantity, H_a can directly be obtained by $\mu_0 H_a = 2K_u/M_s$. Also, the magnetic hardness parameter κ is expressed by [35]

$$\kappa = \left(\frac{K_u}{\mu_0 M_s^2} \right)^{1/2}. \quad (4)$$

The typical hard magnetic materials have κ values often no less than 1 ($\kappa > 1$) [35]. The square and circle symbols in Fig. 5(b) display results of $\mu_0 H_a$ and κ of FeCoN_x for $x \leq 0.5$, respectively. The main trend of K_u of FeCoN_x versus x is well preserved for both $\mu_0 H_a$ and κ , as large K_u and small $\mu_0 M_s$ are favored to enhance them. More specifically, values of $\mu_0 H_a$ and κ increase with x and reach 4.2 T and 1.1 at 20 at. % N, respectively. The corresponding $\mu_0 H_c$'s are thus 0.48–1.17 T when both α and D_{eff} vary within 0.2–0.5. Note that an available experimental $\mu_0 H_c$ of 0.6 T obtained for 10 at. % Al doped FeCo [34] is within this range. Furthermore, depending on the dopant amount, the FeCoN_x could be referred to as semihard ($0.5 < \kappa < 1$) or hard ($\kappa > 1$).

In order to illustrate the origin of K_u , we further decompose K_u into the atom and d -orbital resolved components by the SOC energy difference for the a - and c -axis magnetization, $\Delta E_{\text{soc}} = E_{\text{soc}}^a - E_{\text{soc}}^c$. Here, $E_{\text{soc}} = ((\hbar^2/2m^2c^2)(1/r)[dV(r)/dr]\hat{L} \cdot \hat{S})$, where $V(r)$ is the spherical part of the effective potential within the PAW sphere, and \hat{L} and \hat{S} are orbital and spin operators, respectively. The expectation value of E_{soc} is twice the actual value of the total energy correction to the second order in SOC, i.e., $K_u \approx 1/2\Delta E_{\text{soc}}$ [40,41]. Our calculations indicate that the second-order perturbation theory is a reasonable approximation as the total K_u values overall agree within a few-percent accuracy with those obtained from the atom projected calculations. The other 50% of the SOC energy translates into the crystal-field energy and the formation of the unquenched orbital moment [42]. For $\text{FeCoN}_{0.125}$, we find that $K_u(\text{Fe}_{1\text{N}})$ and $K_u(\text{Co}_{1\text{N}})$ are 0.19 and −0.1 meV, respectively, while $K_u(\text{Fe}_{2\text{N}})$ and $K_u(\text{Co}_{2\text{N}})$ are 0.17 and 0.1 meV. These K_u values of all Fe and Co atoms increase consistently as x increases. Notably, for $x = 0.5$, Fe atoms still provide dominant contributions (0.35 meV), three times more than Co (0.12 meV), to the total K_u .

In Figs. 5(c) and 5(d), we show the d -resolved K_u enhancements of Fe and Co atoms in the presence of N,

$\Delta K_u(X) = K_u(X_{1\text{N}}) - K_u(X_{2\text{N}})$, for $\text{FeCoN}_{0.125}$, respectively. It is obvious, as seen in Fig. 5(c), the $\Delta K_u(\text{Fe})$ arises primarily from the pairs of the short-axis d states coupled by SOC, through the $\langle xy|\hat{L}_z|x^2 - y^2\rangle$ matrix element, as addressed in the perturbation theory [6,7]. These short-axis d orbitals are directly involved in the hybridization with the N-2p electrons on the same a - b plane, as discussed in Fig. 4. On the other hand, the SOC involving the long-axis d orbitals provides small negative contributions. The positive contribution by the $\langle xy|\hat{L}_z|x^2 - y^2\rangle$ decreases significantly in $\Delta K_u(\text{Co})$ [Fig. 5(d)], compared to the Fe, while the other components are more or less preserved.

To get more insight, we show the energy- and k -resolved distribution of the d -orbital band characters of the $\text{Fe}_{1\text{N}}$ and $\text{Co}_{1\text{N}}$ atoms in FeCoN_x in Figs. 6(a)–6(d) for $x = 0$ –0.5, respectively. For simplicity, only the short-axis (on the a - b plane) orbital bands of the d_{xy} and $d_{x^2-y^2}$ states in the minority-spin state are emphasized. For the spin-channel decomposition of K_u , we follow a recipe by the previous full-potential calculations for FeCo with 3.125 at. % N doping, where the spin down-down ($\downarrow\downarrow$) channel contributes predominantly (more than 70%) to the total K_u over the other spin channels, i.e., spin up-down $\uparrow\downarrow$ and up-up $\uparrow\uparrow$ [23]. From the band analyses, we sketch a schematic diagram of the energy levels (ε) of the d_{xy} and

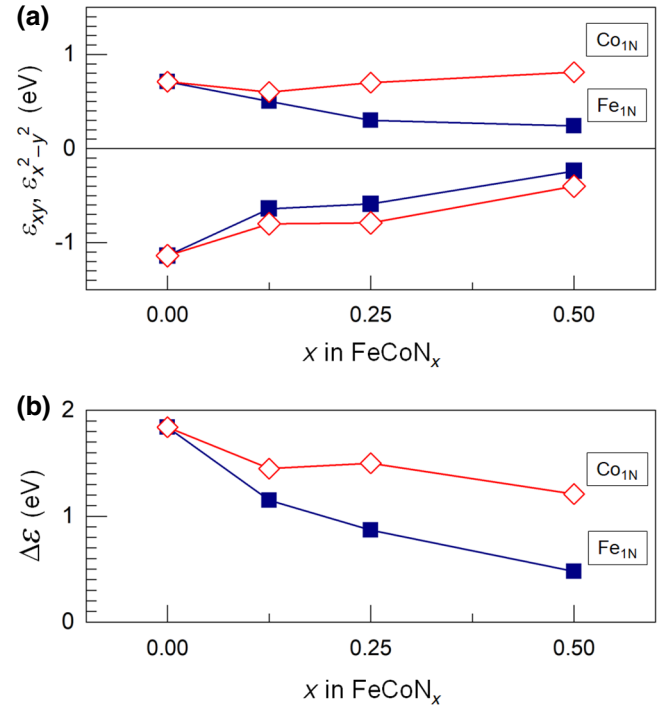


FIG. 7. (a) Energy levels of the occupied $d_{x^2-y^2}$ and unoccupied d_{xy} orbital states relative to E_F at the Γ point of the $\text{Fe}_{1\text{N}}$ (filled) and $\text{Co}_{1\text{N}}$ (unfilled) atoms in FeCoN_x . The Fermi level is set to zero in energy. (b) The absolute value $\Delta\varepsilon$ of the SOC split energy between the occupied $d_{x^2-y^2}$ and unoccupied d_{xy} states of the $\text{Fe}_{1\text{N}}$ (filled) and $\text{Co}_{1\text{N}}$ (unfilled) atoms.

TABLE I. Parameters S_i and S_j and the calculated energy differences Δ_{ij} , Δ_i , and Δ_j (eV), and the exchange constants J_{ij} (meV) of B2 FeCo for different i - j pairs.

	S_i	S_j	Δ_{ij}	Δ_i	Δ_j	J_{ij}
Fe1-Co1	2	3/2	-2.45	-1.38	-1.69	25.8
Fe1-Fe2	2	2	-2.89	-1.38	-1.38	-4.1
Fe1-Fe3	2	2	-3.01	-1.38	-1.38	-7.8
Co1-Co2	3/2	3/2	-3.19	-1.69	-1.69	10.6
Co1-Co3	3/2	3/2	-3.38	-1.69	-1.69	0.2

$d_{x^2-y^2}$ orbital states at the Γ point [Fig. 7(a)]. For B2 FeCo, these d -orbital states of Fe and Co atoms are overlapped at the Γ because of the orbital hybridization between the Fe d and Co d states. When $x > 0$, both the occupied $d_{x^2-y^2}$ and unoccupied d_{xy} states shift toward E_F as x increases. In particular, the E_F -toward shift is more significant in Fe than in Co. The absolute value of the SOC split energy between the occupied and unoccupied states, $\Delta\epsilon = \epsilon_{x^2-y^2} - \epsilon_{xy}$, is also plotted in Fig. 7(b). The $\Delta\epsilon$ value for Fe and Co of B2-FeCo is 1.9 eV. As x increases in FeCoN_x , the $\Delta\epsilon$ decreases and reaches values of 0.5 eV for the $\text{Fe}_{1\text{N}}$ and 1.2 eV for the $\text{Co}_{1\text{N}}$ at $x = 0.5$. The presence of the N dopant develops the strong short-axis orbital hybridization with the Fe atoms in the same a - b plane, rather than with the more isolated Co in the long axis (c axis). We thus conclude that the relative change of the energy split levels in the two short-axis d -orbital states coupled by SOC mainly determines the K_u of (FeCo)N compounds.

From a practical viewpoint, T_c has to be sufficient enough to maintain intrinsic permanent magnetic properties and energy product. We finally estimate T_c using the standard approach in the Heisenberg model of the mean-field approximation according to $T_c = 2J_0/(3k_B)$ [43,44], where J_0 is the exchange coupling integral and k_B is the Boltzmann's constant. From the classical Heisenberg model, the exchange energy per unit cell with N magnetic sublattices can be expressed as [45]

$$E_{\text{ex}} = \frac{1}{2} \sum_{i=1}^N \sum_{j \neq i}^N n_i z_{ij} J_{ij} S_i S_j, \quad (5)$$

where n_i is the number of the i th sublattice, z_{ij} is the number of neighboring sites in the j th sublattice to the i th sublattice, and J_{ij} is the exchange coupling constant between two spins S_i at the i site and S_j at the j site. From the above expression, the exchange integral J_{ij} can then be formulated by [45]

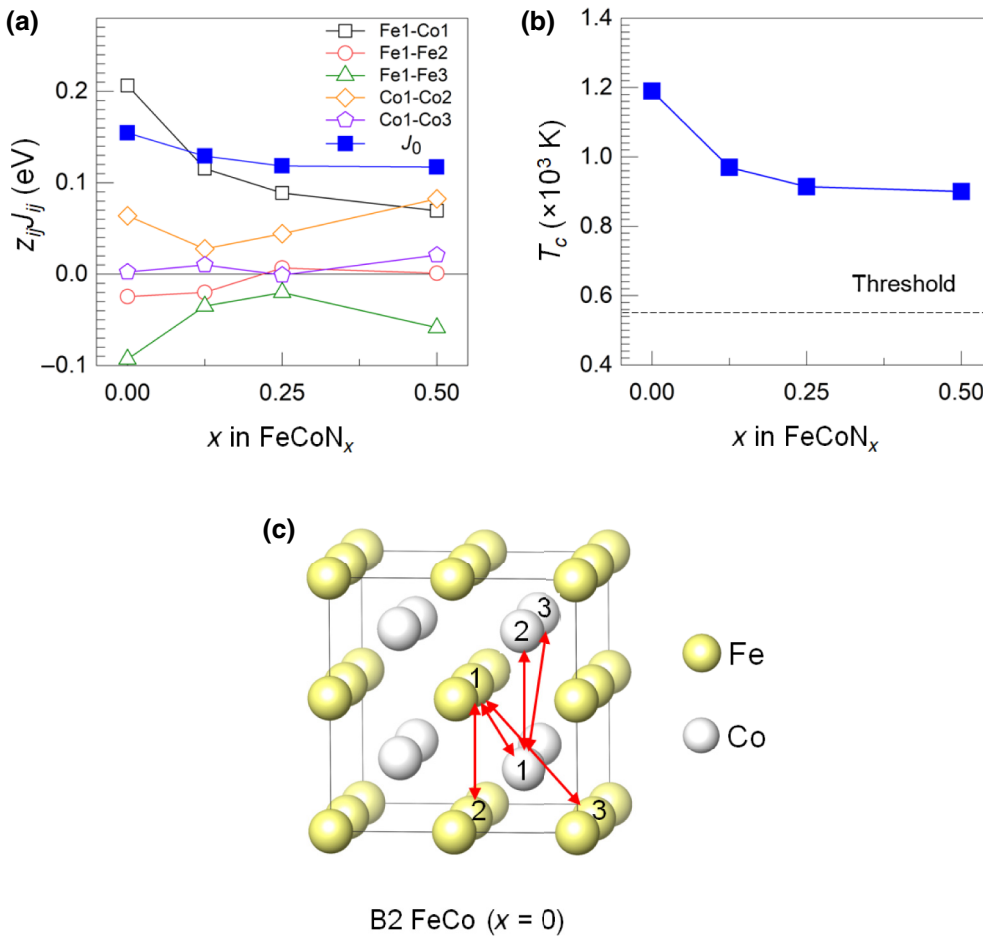
$$J_{ij} = \frac{\Delta_{ij} - \Delta_i - \Delta_j}{4n_i z_{ij} S_i S_j}, \quad (6)$$

where Δ_{ij} is the energy difference between the excited state, where both the spins S_i and S_j in the unit cell are

inverted, and the ground state (i.e., FM), and Δ_i (Δ_j) refers to the spin reorientation of only a single sublattice i (j). To reorient the magnetic moment, we use the constrained local moment approach. In the constrained calculations, we first adjust the magnitude of the Fe and Co moments in B2 FeCo to those obtained from the self-consistent calculations by controlling the Wigner-Seitz radius. The same values of the Wigner-Seitz radius for Fe (0.72 Å) and Co (0.99 Å) atoms are then adapted for all FeCoN_x . For each spin rearrangement, we have fully relaxed the ionic positions while keeping the lattice constants of the ground state FM phase. For reference, we show the parameters S_i and S_j and the calculated values of Δ_{ij} , Δ_i , and Δ_j in Table I for B2 FeCo. All the possible short-range exchange interactions between the different Fe and Co sites within the 3NN are explicitly considered as J_{ij} becomes negligibly small from the 4NN [46]. Thus, J_0 is linear combinations of $J_{ij}^{1\text{NN}}$, $J_{ij}^{2\text{NN}}$, $J_{ij}^{3\text{NN}}$, and $J_0 = \sum_{k=1}^3 z_{ij}^{k\text{NN}} J_{ij}^{k\text{NN}}$.

We first inspect the validity of our calculations of J_0 and T_c with the reference system, bcc-Fe. For bcc-Fe, we find that values of $J_{\text{Fe-Fe}}^{1\text{NN}}$, $J_{\text{Fe-Fe}}^{2\text{NN}}$, and $J_{\text{Fe-Fe}}^{3\text{NN}}$ are 16.8, 0.9, and -1.4 meV, respectively. The positive and negative values of J_{ij} indicate the preference of parallel and antiparallel couplings of S_i and S_j , respectively. With $z_{\text{Fe-Fe}}^{1\text{NN}} = 8$, $z_{\text{Fe-Fe}}^{2\text{NN}} = 6$, and $z_{\text{Fe-Fe}}^{3\text{NN}} = 12$, $J_0 = 0.124$ eV and $T_c = 962$ K for bcc-Fe. Our T_c is in reasonable agreement with the previous theories (900–1200 K) [43,47,48] and experiments (1040–1045 K) [49–51]. Results of J_0 and T_c for FeCoN_x are shown in Figs. 8(a) and 8(b) for $x \leq 0.5$, respectively. In Fig. 8(a), we also show the calculated values of the normalized exchange parameters, namely, $z_{\text{Fe1-Co1}}^{1\text{NN}} J_{\text{Fe1-Co1}}^{1\text{NN}}$, $z_{\text{Fe1-Fe2}}^{2\text{NN}} J_{\text{Fe1-Fe2}}^{2\text{NN}}$, $z_{\text{Co1-Co2}}^{2\text{NN}} J_{\text{Co1-Co2}}^{2\text{NN}}$, $z_{\text{Fe1-Fe3}}^{3\text{NN}} J_{\text{Fe1-Fe3}}^{3\text{NN}}$, and $z_{\text{Co1-Co3}}^{3\text{NN}} J_{\text{Co1-Co3}}^{3\text{NN}}$, in the unfilled symbols. For better visualization, the schematic of these exchange couplings is illustrated in Fig. 8(c) for B2 FeCo. Note that, for the cases of $x > 0$, where $c/a > 1$, the exchange interactions along the c and a axes are not identical.

For B2 FeCo, we find that the calculated values of J_0 and T_c are 0.155 eV and 1195 K, respectively. As shown in Fig. 8(a), $J_{\text{Fe1-Co1}}^{1\text{NN}}$ and $J_{\text{Co1-Co2}}^{2\text{NN}}$ provide positive contributions to J_0 , whereas $J_{\text{Fe1-Fe2}}^{2\text{NN}}$ and $J_{\text{Fe1-Fe3}}^{3\text{NN}}$ do contribute negatively. More specifically, while the dominant contribution to J_0 comes mainly from the 1NN interaction ($J_{\text{Fe1-Co1}}^{1\text{NN}}$), the 2NN and 3NN interactions cannot be ignored for determining J_0 and T_c . Notably, our predicted T_c agrees (within 5%) with an experimental value of 1253 K [52,53], superior to the previous calculations ($T_c = 1660$ –1670 K) that take into account only the 1NN Fe-Co interaction [47]. In a trend similar to $J_{\text{Fe1-Co1}}^{1\text{NN}}$, both J_0 and T_c of FeCoN_x decrease with x , reaching their minima of $J_0 = 0.117$ eV and $T_c = 905$ K at $x = 0.5$. Values of T_c (905–1195 K) of (FeCo)N compounds thus fulfill the basic requirement of high-performance permanent magnetic materials ($T_c >$



550 K), as proposed in Ref. [54]. The enhanced tetragonal distortion and volume expansion by the N dopants could cause reduction of the exchange interactions and Curie temperature, as the neighboring magnetic moments weaken effects (such as the overlap of 3d wave functions) when separated farther [46].

IV. CONCLUSION

In summary, we report results of first-principles calculations on an unexpectedly large uniaxial magnetic anisotropy up to approximately 0.5 meV/f.u. with the easy magnetization along the long-axis direction in B2-ordered tetragonal FeCo. The present study provides a viable route to achieve intrinsic hard magnetic properties (i.e., large magnetization and uniaxial magnetic anisotropy at the same time) by breaking the high-symmetry structure with a suitable interstitial doping of 2p-electron elements. Through single-particle energy spectra analyses with spin-orbit Hamiltonian matrix elements, the underlying mechanism is discussed in connection with the substantial changes in the spin-orbit coupled d-orbital states projected on the short-axis plane, d_{xy} and $d_{x^2-y^2}$, induced by the large tetragonal distortion and the strong 3d-2p hybridization. We hope that our prediction inspires subsequent

experimental investigations of rare-earth or heavy-metal free high-performance permanent magnets and spintronics materials.

ACKNOWLEDGMENTS

This research was supported by the Future Materials Discovery Program through the National Research Foundation of Korea (NRF) funded by the Ministry of Science and ICT (Grant No. 2016M3D1A1027831).

- [1] T. Klemmer, D. Hoydick, H. Okumura, B. Zhang, and W. A. Soffa, Magnetic hardening and coercivity mechanisms in L10 ordered FePd ferromagnets, *Scr. Metall. Mater.* **33**, 1793 (1995).
- [2] V. Gehanno, A. Marty, B. Gilles, and Y. Samson, Magnetic domains in epitaxial ordered FePd(001) thin films with perpendicular magnetic anisotropy, *Phys. Rev. B* **55**, 12552 (1997).
- [3] S. Okamoto, N. Kikuchi, O. Kitakami, T. Miyazaki, Y. Shimada, and K. Fukamichi, Chemical-order-dependent magnetic anisotropy and exchange stiffness constant of FePt(001) epitaxial films, *Phys. Rev. B* **66**, 024413 (2002).

- [4] K. Barmak, J. Kim, L. H. Lewis, K. R. Coffey, M. F. Toney, A. J. Kellock, and J.-U. Thiele, On the relationship of magnetocrystalline anisotropy and stoichiometry in epitaxial L10 CoPt (001) and FePt (001) thin films, *J. Appl. Phys.* **98**, 033904 (2005).
- [5] D. Odkhuu, S. H. Rhim, N. Park, K. Nakamura, and S. C. Hong, Jahn-Teller driven perpendicular magnetocrystalline anisotropy in metastable ruthenium, *Phys. Rev. B* **91**, 014437 (2015).
- [6] P. Bruno, Tight-binding approach to the orbital magnetic moment and magnetocrystalline anisotropy of transition-metal monolayers, *Phys. Rev. B* **39**, 865 (1989).
- [7] D. S. Wang, R. Q. Wu, and A. J. Freeman, First-principles theory of surface magnetocrystalline anisotropy and the diatomic-pair model, *Phys. Rev. B* **47**, 14932 (1993).
- [8] T. Burkert, L. Nordstrom, O. Eriksson, and O. Heinonen, Giant Magnetic Anisotropy in Tetragonal FeCo Alloys, *Phys. Rev. Lett.* **93**, 027203 (2004).
- [9] A. Winkelmann, M. Przybylski, F. Luo, Y. Shi, and J. Barthel, Perpendicular Magnetic Anisotropy Induced by Tetragonal Distortion of FeCo Alloy Films Grown on Pd(001), *Phys. Rev. Lett.* **96**, 257205 (2006).
- [10] F. Yildiz, M. Przybylski, X.-D. Ma, and J. Kirschner, Strong perpendicular anisotropy in $Fe_{1-x}Co_x$ alloy films epitaxially grown on mismatching Pd(001), Ir(001), and Rh(001) substrates, *Phys. Rev. B* **80**, 064415 (2009).
- [11] G. Andersson, T. Burkert, P. Warnicke, M. Bjorck, B. Sanyal, C. Chacon, C. Zlotea, L. Nordstrom, P. Nordblad, and O. Eriksson, Perpendicular Magnetocrystalline Anisotropy in Tetragonally Distorted Fe-Co Alloys, *Phys. Rev. Lett.* **96**, 037205 (2006).
- [12] P. E. Blöchl, Projector augmented-wave method, *Phys. Rev. B* **50**, 17953 (1994).
- [13] G. Kresse and J. Furthmüller, Efficient iterative schemes for ab initio total-energy calculations using a plane-wave basis set, *Phys. Rev. B* **54**, 11169 (1996).
- [14] J. P. Perdew, K. Burke, and M. Ernzerhof, Generalized Gradient Approximation Made Simple, *Phys. Rev. Lett.* **77**, 3865 (1996).
- [15] H. Y. Wang, E. Y. Jiang, Z. W. Ma, Y. J. He, and H. S. Huang, The effect of annealing on the structure and magnetic properties of FeCoN thin films, *J. Phys.: Condens. Matter* **11**, 989 (1998).
- [16] E. Y. Jiang, H. Y. Wang, and Z. W. Ma, The effect of Co addition on the saturation magnetization of $Fe_{16}N_2$, *J. Appl. Phys.* **85**, 4488 (1999).
- [17] A. Yang, H. Imrane, J. Lou, J. Kirkland, C. Vittoria, N. Sun, and V. G. Harris, Effects of boron addition to the atomic structure and soft magnetic properties of FeCoB films, *J. Appl. Phys.* **103**, 07E736 (2008).
- [18] K. H. Jack, The occurrence and the crystal structure of α -iron nitride: A new type of interstitial alloy formed during the tempering of nitrogen-martensite, *Proc. R. Soc. A* **208**, 216 (1951).
- [19] M. Chandran, L. E. Iorio, and P. R. Subramanian, Effect of nitrogen on the magnetic moment of α -Fe and FeCo alloys from first-principle calculations, *J. Appl. Phys.* **101**, 033912 (2007).
- [20] D. D. Koelling and B. N. Harmon, A technique for relativistic spin-polarised calculations, *J. Phys. C Solid State* **10**, 3107 (1977).
- [21] S. P. Ong, L. Wang, B. Kang, and G. Ceder, Li-Fe-P-O2 Phase Diagram from First Principles Calculations, *Chem. Mater.* **20**, 1798 (2008).
- [22] S. P. Ong, A. Jain, G. Hautier, B. Kang, and G. Ceder, Thermal stabilities of delithiated olivine MPO4 ($M = Fe, Mn$) cathodes investigated using first principles calculations, *Electrochim. Commun.* **12**, 427 (2010).
- [23] I. Khan and J. Hong, Magnetic anisotropy of C and N doped bulk FeCo alloy: A first principles study, *J. Magn. Magn. Mater.* **388**, 101 (2015).
- [24] M. Neumayer and M. Fahnle, Atomic defects in FeCo: Stabilization of the B2 structure by magnetism, *Phys. Rev. B* **64**, 132102 (2001).
- [25] L. Bornstein, *Numerical Data and Functional Relationships in Science and Technology*, New Series, edited by K.-H. Hellwege (Springer, New York, 1979).
- [26] R. M. Bozorth, *Ferromagnetism* (Van Nostrand, New York, 1951).
- [27] D. I. Bardos, Mean Magnetic Moments in bcc FeCo Alloys, *J. Appl. Phys.* **40**, 1371 (1969).
- [28] D. Wu, Q. Zhang, J. P. Liu, D. Yuan, and R. Q. Wu, First-principles prediction of enhanced magnetic anisotropy in FeCo alloys, *Appl. Phys. Lett.* **92**, 052503 (2008).
- [29] M. Sagawa, S. Fujimura, H. Yamamoto, Y. Matsuura, and S. Hirosawa, Magnetic properties of rare-earth-iron-boron permanent magnet materials, *J. Appl. Phys.* **57**, 4094 (1985).
- [30] E. K. Delczeg-Czirjak, A. Edstrom, M. Werwinski, J. Rusz, N. V. Skorodumova, L. Vitos, and O. Eriksson, Stabilization of the tetragonal distortion of Fe_xCo_{1-x} alloys by C impurities: A potential new permanent magnet, *Phys. Rev. B* **89**, 144403 (2014).
- [31] M. Kim and A. J. Freeman, Hybridization reduction of the magnetization for N-doped FeCo superlattices, *Appl. Phys. Lett.* **82**, 3484 (2003).
- [32] M. Weinert, R. E. Watson, and J. W. Davenport, Total-energy differences and eigenvalue sums, *Phys. Rev. B* **32**, 2115 (1985).
- [33] Y. Kota and A. Sakuma, Degree of order dependence on magnetocrystalline anisotropy in body-centered tetragonal FeCo alloys, *Appl. Phys. Express* **5**, 113002 (2012).
- [34] T. Hasegawa, S. Kanatani, M. Kazaana, K. Takahashi, K. Kumagai, M. Hirao, and S. Ishio, Conversion of FeCo from soft to hard magnetic material by lattice engineering and nanopatterning, *Sci. Rep.* **7**, 13215 (2017).
- [35] R. Skomski and J. M. D. Coey, Magnetic anisotropy – How much is enough for a permanent magnet?, *Scripta Mater.* **112**, 3 (2016).
- [36] H. Kronmüller, Theory of nucleation fields in inhomogeneous ferromagnets, *Phys. Status Solidi B* **144**, 385 (1987).
- [37] H. Kronmüller, K. D. Durst, and M. Sagawa, Analysis of the magnetic hardening mechanism in RE-FeB permanent magnets, *J. Magn. Magn. Mater.* **74**, 291 (1988).
- [38] J. Fischbacher, A. Kovacs, L. Exl, J. Kühnel, E. Mehofer, H. S. Amin, T. Ohkubo, K. Hono, and T. Schrefl, Searching the weakest link: Demagnetizing fields and magnetization reversal in permanent magnets, *Scripta Mater.* **154**, 253 (2018).
- [39] J. Fischbacher, A. Kovacs, M. Gusenbauer, H. Oezelt, L. Exl, S. Bance, and T. Schrefl, Micromagnetics of rare-earth

- efficient permanent magnets, *J. Phys. D: Appl. Phys.* **51**, 193002 (2018).
- [40] V. Antropov, L. Ke, and D. Aberg, Constituents of magnetic anisotropy and a screening of spin-orbit coupling in solids, *Solid State Comm.* **194**, 35 (2014).
- [41] J. Zhang, P. V. Lukashev, S. S. Jaswal, and E. Y. Tsymbal, Model of orbital populations for voltage-controlled magnetic anisotropy in transition-metal thin films, *Phys. Rev. B* **96**, 014435 (2017).
- [42] R. Skomski, A. Kashyap, and A. Enders, Is the magnetic anisotropy proportional to the orbital moment?, *J. Appl. Phys.* **109**, 07E143 (2011).
- [43] A. I. Liechtenstein, M. I. Katsnelson, V. P. Antropov, and V. A. Gubanov, Local spin density functional approach to the theory of exchange interactions in metals and alloys, *J. Magn. Magn. Mater.* **67**, 65 (1987).
- [44] S. V. Halilov, H. Eschrig, A. Y. Perlov, and P. M. Oppeneer, Adiabatic spin dynamics from spin-density-functional theory: Application to Fe, Co, and Ni, *Phys. Rev. B* **58**, 293 (1998).
- [45] P. Novak and J. Rusz, Exchange interactions in barium hexaferrite, *Phys. Rev. B* **71**, 184433 (2005).
- [46] A. Jakobsson, E. Sasioglu, Ph. Mavropoulos, M. Lezaic, B. Sanyal, G. Bihlmayer, and S. Blugel, Tuning the Curie temperature of FeCo compounds by tetragonal distortion, *Appl. Phys. Lett.* **103**, 102404 (2013).
- [47] M. Lezaic, Ph. Mavropoulos, and S. Blugel, First-principles prediction of high Curie temperature for ferromagnetic bcc-Co and bcc-FeCo alloys and its relevance to tunneling magnetoresistance, *Appl. Phys. Lett.* **90**, 082504 (2007).
- [48] M. Pajda, J. Kudrnovsky, I. Turek, V. Drchal, and P. Bruno, Ab initio calculations of exchange interactions, spin-wave stiffness constants, and Curie temperatures of Fe, Co, and Ni, *Phys. Rev. B* **64**, 174402 (2001).
- [49] J. Crangle and G. M. Goodman, The magnetization of pure iron and nickel, *Proc. Roy. Soc. A* **321**, 477 (1971).
- [50] R. Pauthenet, Spin-waves in nickel, iron, and yttrium-iron garnet, *J. Appl. Phys.* **53**, 2029 (1982); **53**, 8187 (1982).
- [51] J. M. Leger, C. Loriers-Susse, and B. Vodar, Pressure effect on the curie temperatures of transition metals and alloys, *Phys. Rev. B* **6**, 4250 (1972).
- [52] R. M. Bozorth, *Ferromagnetism* (Van Nostrand Reinhold Inc., U.S., 1951).
- [53] R. S. Sundar and S. C. Deevi, Soft magnetic FeCo alloys: Alloy development, processing, and properties, *Int. Mater. Rev.* **50**, 157 (2005).
- [54] J. M. D. Coey, Permanent magnets: Plugging the gap, *Scripta Mater.* **67**, 524 (2012).